

The role of three-dimensional transport in driving enhanced electron acceleration during magnetic reconnection

J. T. Dahlin,^{1, a)} J. F. Drake,^{1, b)} and M. Swisdak¹

*Institute for Research in Electronics and Applied Physics,
University of Maryland, College Park, Maryland 20742,
USA*

Magnetic reconnection is an important driver of energetic particles in many astrophysical phenomena. Using kinetic particle-in-cell (PIC) simulations, we explore the impact of three-dimensional reconnection dynamics on the efficiency of particle acceleration. In two-dimensional systems, Alfvénic outflows expel energetic electrons into flux ropes where they become trapped and disconnected from acceleration regions. However, in three-dimensional systems these flux ropes develop axial structure that enables particles to leak out and return to acceleration regions. This requires a finite guide field so that particles may move quickly along the flux rope axis. We show that greatest energetic electron production occurs when the guide field is of the same order as the reconnecting component: large enough to facilitate strong transport, but not so large as to throttle the dominant Fermi mechanism responsible for efficient electron acceleration. This suggests a natural explanation for the envelope of electron acceleration during the impulsive phase of eruptive flares.

PACS numbers: 52.35.Vd, 94.30.cp, 52.65.Rr, 96.60.Iv

^{a)}University Corporation for Atmospheric Research, Boulder, CO, USA; NASA Goddard Space Flight Center, Greenbelt, Maryland 20771, USA; Jack Eddy Postdoctoral Fellow; joel.t.dahlin@nasa.gov

^{b)}Department of Physics, University of Maryland, College Park, Maryland 20742, USA; Institute for Physical Science and Technology, University of Maryland, College Park, Maryland 20742, USA

I. INTRODUCTION

Magnetic reconnection is thought to be an important driver of energetic particles in astrophysical plasmas, releasing stored magnetic energy via efficient acceleration of a non-thermal population. Reconnection-associated energetic particle production has been well-observed in solar flares¹ and magnetospheric storms². Solar flare observations in particular indicate that reconnection-driven acceleration can be very efficient, driving a large non-thermal electron component with a total energy content comparable to that of the energy in the initial magnetic field^{3,4}. This mechanism therefore provides a promising explanation for a variety of astrophysical phenomena characterized by energetic particle production, including stellar flares, gamma-ray bursts^{5,6}, and gamma-ray flares in pulsar wind nebulae^{7,8}.

Electron acceleration by magnetic reconnection has attracted significant interest, e.g.^{9–15}. Two specific processes have received the most attention. The first is acceleration by electric fields parallel to the local magnetic field (E_{\parallel})^{11,16–18}. However, the number of electrons that can be accelerated through this mechanism can be limited because during magnetic reconnection non-zero E_{\parallel} typically only occur near X-lines and separatrices. Additionally, acceleration by parallel electric fields has a weak energy-scaling¹⁹ ($\sim \epsilon^{1/2}$ with ϵ the particle energy) and characteristically drives bulk electron heating rather than a non-thermal component.

In the second process²⁰, charged particles gain energy as they reflect from the ends of contracting magnetic islands. (An analogous process occurs during the acceleration of cosmic rays by the first-order Fermi mechanism.) In contrast to the localization of E_{\parallel} , this can occur wherever there are contracting field lines, including the merging of magnetic islands and in the outflows of single X-line reconnection^{14,15,20–22} and in turbulent reconnecting systems where magnetic field lines are stochastic and conventional islands do not exist¹⁹. This mechanism is therefore volume-filling and can accelerate a large number of particles. This mechanism scales strongly with the particle energy ($\sim \epsilon$) and preferentially energizes non-thermal particles^{19,23}.

Several recent studies of two-dimensional reconnection^{23–25} found that the guide field (the magnetic component parallel to the reconnection axis) controls which mechanisms contribute to electron energy gain. In the antiparallel (small guide field) regime Fermi reflection dominates^{23–27}, whereas in reconnection where the guide field is much larger than the recon-

necting component parallel electric fields drive essentially all of the electron energy gain^{23,28}. In the latter (strong guide field) regime energetic electron production is weak, indicating that parallel electric fields are ineffective drivers of energetic electrons in reconnection²³.

Studies of particle acceleration in reconnection have primarily been based on 2D simulations, in which accelerated particles are typically localized near the X-line, along magnetic separatrices and within magnetic islands^{11,26}. There are some observations with small ambient guide fields^{29–31} that support such a picture. A notable exception are Wind observations in which energetic electrons up to 300 keV are seen for more than an hour in an extended region around the reconnection region². These observations correspond to reconnection with a strong guide field.

Two-dimensional simulations impose limitations on the magnetic topology as well as the available spectrum of instabilities. In the presence of an ambient guide field, 3D reconnection can become turbulent as a result of the generation of magnetic islands along separatrices and adjacent surfaces^{32,33}. While test particle trajectories in MHD fields have been used to explore acceleration in such systems^{34,35}, the absence of feedback of energetic particles on the reconnection process in such models limits their applicability to physical systems. Recent 3D studies of kinetic reconnection examined particle acceleration in pair plasmas^{26,36}. However, these studies focused on relativistic regimes where the magnetic energy per particle exceeds the rest mass energy and included no ambient guide field.

In a recent kinetic study of nonrelativistic reconnection, we showed that energetic electron production was greatly enhanced in three-dimensional systems¹⁹. This occurs because two-dimensional magnetic islands trap particles, limiting energy gain, whereas three-dimensional reconnection generates a stochastic field that enables electrons to access volume-filling acceleration regions. The relative enhancement was found to increase with the size of the simulation domain, suggesting that the impact of three-dimensional dynamics is robust for astrophysical characterized by spatial and temporal scales that are much larger than kinetic scales.

In this article, we extend this study in several key ways. We begin by reviewing the theory of particle acceleration in reconnection (section II) and describing our kinetic particle-in-cell (PIC) simulations (section III). We then explore the physics of two and three-dimensional reconnection to highlight the remarkable similarity of many of the bulk properties (section IV). In section V, we review the physics of electron acceleration enhancement in 3D

reconnection and demonstrate, by varying the spatial length in the third dimension, that transport and enhanced acceleration are intrinsically linked. We show in section VI that a magnetic guide field plays an important role in facilitating three-dimensional transport, and in section VII introduce an ‘injection criterion’ that explains why energetic electrons are enhanced but protons are not. We discuss the astrophysical implications of these results in section VIII.

II. PARTICLE ACCELERATION IN THE GUIDING-CENTER LIMIT

In order to examine electron acceleration we assume a guiding-center approximation relevant for a strong guide field^{19,37}. In this limit, the evolution of the kinetic energy ϵ of a single electron can be written as:

$$\frac{d\epsilon}{dt} = qE_{\parallel}v_{\parallel} + \frac{\mu}{\gamma} \left(\frac{\partial B}{\partial t} + \mathbf{u}_E \cdot \nabla B \right) + \gamma m_e v_{\parallel}^2 (\mathbf{u}_E \cdot \boldsymbol{\kappa}) \quad (1)$$

where $E_{\parallel} = \mathbf{E} \cdot \mathbf{b}$ is the parallel electric field, $\mu = m_e \gamma^2 v_{\perp}^2 / 2B$ is the magnetic moment, $\mathbf{u}_E = c\mathbf{E} \times \mathbf{B} / B^2$, and $\boldsymbol{\kappa} = \mathbf{b} \cdot \nabla \mathbf{b}$ is the magnetic curvature. The velocity components parallel and perpendicular to the magnetic field are v_{\parallel} and v_{\perp} , respectively; γ is the relativistic Lorentz factor, and \mathbf{b} is the unit vector in the direction of the local magnetic field.

The first term on the right-hand-side of the equation corresponds to acceleration by parallel electric fields, which are typically localized near the reconnection X-line and along separatrices. The second term corresponds to betatron acceleration associated with μ conservation in a temporally and spatially varying magnetic field. Because reconnection releases a system’s magnetic energy, this typically causes electron cooling²⁴. The last term corresponds to Fermi reflection of particles from contracting magnetic field lines^{15,20,21,24}. Both E_{\parallel} and Fermi reflection change the parallel energy of the particles, while betatron acceleration changes the perpendicular energy. The term $\mathbf{u}_E \cdot \boldsymbol{\kappa}$ corresponds to local field line contraction: $\mathbf{u}_E \cdot \boldsymbol{\kappa} = -\dot{\ell}/\ell$ (where ℓ is the field line length) and is linked to the conservation of the parallel adiabatic invariant $\int v_{\parallel} d\ell$. The guiding-center approximation given in Eq. (1) is accurate when electrons are well-magnetized. In the weak-guide field regime, other terms such as the polarization drift may be significant (compare Li et al.²⁷). However, the polarization drift gives the change in the electron bulk flow energy which is typically small for a realistic electron-to-ion mass ratio.

III. PARTICLE-IN-CELL SIMULATIONS

We explore particle acceleration in reconnection via simulations using the massively parallel 3D particle-in-cell (PIC) code `p3d`³⁸. Particle trajectories are calculated using the relativistic Newton-Lorentz equation, and the electromagnetic fields are advanced using Maxwell's equations. The time and space coordinates are normalized, respectively, to the proton cyclotron time $\Omega_{ci}^{-1} = m_i c / e B_{x0}$ and inertial length $d_i = c / \omega_{pi}$. The typical grid cell width $\Delta = d_e / 4$, where $d_e = d_i \sqrt{m_e / m_i}$ is the electron inertial length. The time step is $dt = \Omega_{ce}^{-1} / 4$, where $\Omega_{ce} = (m_i / m_e) \Omega_{ci}$ is the electron cyclotron frequency.

All simulations are initialized with a force-free configuration and use periodic boundary conditions. This is chosen as the most generic model for large-scale systems such as the solar corona where the density jump between the current layer and upstream plasma is not expected to be important. The magnetic field is given by $B_x = B_{x0} \tanh(y/w_0)$ and $B_z = \sqrt{(1 + b_g^2) B_{x0}^2 - B_x^2}$, corresponding to an asymptotic guide field $B_{z0} = b_g B_{x0}$. We include two current sheets at $y = L_y/4$ and $3L_y/4$ to produce a periodic system, and choose $w_0 = 1.25d_e$. This initial configuration is not a kinetic equilibrium, which would require a temperature anisotropy³⁹, but is in pressure balance. We use at least 50 particles per cell per species. The initial electron and proton temperatures are equal and isotropic with $T_0 = 0.25m_i c_A^2$, and the initial density n_0 and pressure P are constant so that $\beta_x = 8\pi P / B_{x0}^2 = 0.5$. The speed of light is $c = 3c_A \sqrt{m_i / m_e}$, where $c_A = B_{x0} / \sqrt{4\pi m_i n_0}$ is the Alfvén speed based on the reconnecting component of the magnetic field.

Table I lists the simulation configurations discussed in this paper. We focus on configurations SM ('medium') and SL ('large') with spatial dimensions $L_x \times L_y = 51.2d_i \times 25.6d_i$ and $L_x \times L_y = 102.4d_i \times 51.2d_i$, respectively. The larger simulations (SL) have more magnetic flux to reconnect, and can therefore run for a longer time and generate many more energetic electrons. However, the SM configuration is ~ 8 times less expensive and therefore better suited for parameter scans. Except where noted, the simulations are performed with a guide field $b_g = 1$ and the three-dimensional simulations use $L_z/d_i = 25.6$ (as in Dahlin et al., 2015¹⁹). The simulation with $b_g = 1.5$ in configuration SM uses $\Delta/d_e = \Omega_{ce} dt = 1/6$. The electron-positron (pair plasma) configuration (S1) uses $\Omega_{ce} dt = 1/20$ and $\Delta/d_e = 1/4$.

The PIC formulation results in some numerical heating that can differ between 2D and 3D domains. To simplify comparisons of particle energization, we perform a set of simula-

Name	L_x/d_i	L_y/d_i	L_z/d_i	m_i/m_e	b_g
SM	51.2	25.6	2D, 1.6 - 25.6	25	0 - 1.5
SL	102.4	51.2	2D, 1.6, 25.6	25	0, 0.5, 1.0
S1	102.4	51.2	1.6, 51.2	1	1.0
S100	51.2	25.6	0.8, 25.6	100	1.0

TABLE I. Simulation Parameters.

tions with $L_z \sim 1.6d_i \ll L_x, L_y$ so that the numerical heating is the same as in 3D, yet the reconnection physics remains essentially 2D (see Section V and Fig. 7). To reduce computational expense, configurations SM and SL have an artificial proton-to-electron mass ratio $m_i/m_e = 25$. Simulations with $m_i/m_e = 100$ (S100) and $m_i/m_e = 1$ (S1) are also presented to explore the impact of the separation between electron and proton scales.

IV. OVERVIEW OF RECONNECTION IN 2D AND 3D DOMAINS

Reconnection develops from particle noise via the tearing instability, which generates interacting flux ropes that grow and merge until they reach the system size. These tearing modes grow wherever $\mathbf{k} \cdot \mathbf{B} = 0$ (Ref. 40). In a slab equilibrium with $\mathbf{B} = B_x(y)\mathbf{x} + B_z(y)\mathbf{z}$, such modes are characterized by a wavevector $\mathbf{k} = k_x\mathbf{x} + k_z\mathbf{z}$ and grow on flux surfaces defined by $B_x/B_z = -k_z/k_x$. The pitch of the unstable mode is given by a characteristic angle $\theta = \arctan(k_z/k_x)$ with respect to the reconnecting field B_x . In a two-dimensional system where $k_z = d/dz = 0$, tearing modes are constrained to grow at the center of the current sheet where $B_x = 0$. However, in three-dimensional systems the nonlinear interaction of modes with different pitches destroys flux surfaces and generates a stochastic, turbulent magnetic field that facilitates enhanced particle transport^{33,41}.

This stochastic magnetic structure is illustrated in Figs. 1a-b, which show isosurfaces of one component of the electron current density J_{ez} in configuration SM. At $t = 12$, several tearing structures with $k_z \neq 0$ are visible (compare Fig. 1 in Daughton et al. 2011³³). The filamentary current distribution at $t = 50$ showcases the late-time nonlinear development. A different view of the filamentary structure, which emphasizes the stochastic structure of the magnetic field, can be observed in the Poincaré surface-of-section shown in Figure 1c. There is a clear boundary between the stochastic reconnecting region (disordered punctures) and

the asymptotic, laminar field.

The stochastic 3D dynamics do not substantially impact the magnetic energy release (see Fig. 2a), as has been noted by Daughton et al.⁴² Another diagnostic for the energy release is the field-line contraction $\mathbf{u}_E \cdot \boldsymbol{\kappa}$ that drives Fermi acceleration according to Eq. (1). The spatial average $\langle \mathbf{u}_E \cdot \boldsymbol{\kappa} \rangle$, (calculated over the stochastic reconnection region described below) is shown in Fig. 2b. Although the 2D simulation is relatively bursty, the overall time-evolution is comparable to that in 3D. In both simulations, $\langle \mathbf{u}_E \cdot \boldsymbol{\kappa} \rangle$ decreases in time as islands grow and the typical radius of curvature $R_c = |\boldsymbol{\kappa}|^{-1}$ increases. Figure 2c shows the probability distribution function (pdf) of $\mathbf{u}_E \cdot \boldsymbol{\kappa}$ inside the stochastic reconnecting region at $\Omega_{ci}t = 40$. The pdf in the 3D system is symmetric for small values of $\mathbf{u}_E \cdot \boldsymbol{\kappa}$, and is consistent with a double-exponential distribution $\propto \exp[-|\mathbf{u}_E \cdot \boldsymbol{\kappa}| \tau_A / 0.39]$ where $\tau_A = L_x / c_A$ is the Alfvén crossing time. The symmetric component can only produce net acceleration through a second-order Fermi process. The positive mean value $\langle \mathbf{u}_E \cdot \boldsymbol{\kappa} \rangle \tau_A \approx 0.2$ is due to the large positive tail visible for $(\mathbf{u}_E \cdot \boldsymbol{\kappa}) \tau_A > 1$. Although the characteristic scales for first and second-order components are comparable, the first-order mechanism is far more efficient, and hence is the dominant driver of particle acceleration in this system. The symmetric (second-order Fermi) component is consistent with Alfvénic fluctuations where the flow and curvature are out of phase corresponding to no net field-line contraction, i.e. $\langle \mathbf{u}_E \cdot \boldsymbol{\kappa} \rangle = 0$.

It has been shown previously that the development of pressure anisotropy with $P_{\parallel} \gg P_{\perp}$ causes the cores of magnetic islands to approach firehose marginal stability, where the tension driving magnetic reconnection ceases, thereby throttling reconnection^{20,21,43}. Figure 3a,c show that a significant anisotropy $P_{\parallel} > P_{\perp}$ develops, as is the typical case in 2D (not shown). This suggests that the plasma heating and energization occurs in similar ways in 2D and 3D, and that the turbulent magnetic field generated in 3D does not isotropize the plasma. Phase space plots of temperature anisotropy T_{\parallel}/T_{\perp} and $\beta_{\parallel} = 8\pi P_{\parallel}/B^2$ are shown in Fig. 4 for three values of the guide field b_g in 2D and 3D, along with marginal stability boundaries for the firehose and mirror instabilities (bottom and top, respectively) in a similar format to that used previously in analyzing solar wind data^{44,45}. For the strong guide field cases (4e,f) there is insufficient free energy in the reconnecting field to drive the system either firehose or mirror unstable. However, for the simulations with $b_g = 0.2, 0.5$ (Fig. 4a-d) the phase space brushes up against the stability boundaries. Hence, feedback of heating on reconnection via anisotropy-driven instabilities can occur in 3D systems.

Reconnection primarily drives electron acceleration parallel to the local magnetic field, generating superthermal particles that fill the stochastic reconnecting region¹⁹. The presence of reconnection-accelerated electrons is therefore a useful proxy for the reconnection region. This is similar to the “electron mixing” described by Daughton et al. (Ref. 42). Indeed, the volume defined by $P_{e\parallel,nt} \geq 0.04n_0T_{e0}$ (where $P_{e\parallel,nt}$ is the parallel energy density of electrons exceeding $\epsilon = 0.2m_e c^2$) corresponds well to the reconnecting region as indicated by the electron pressure and current density (see Fig. 3). Using this marker for designating the reconnection domain allows us to estimate the reconnected volume V_r and can be used to determine a characteristic width in the 3D system: $L_r = V_r/L_x L_z$. The 2D analogue is the area inside the separatrices of the primary X-line. A mean inflow velocity can then be determined from $v_{in} = \dot{L}_r/2$, yielding comparable $v_{in}/c_A \approx 0.057, 0.045$ for the 3D and 2D simulations respectively (\dot{L}_r is averaged from $\Omega_{ci}t = 8$ to $\Omega_{ci}t = 125$). A calculation of the 2D reconnection rate, determined from the time rate of change of the flux function at the primary X-line, yields a nearly identical inflow velocity $v_{in}/c_A \approx 0.049$. Figure 2d shows that the width of the reconnecting region is comparable to the mean radius of curvature, consistent with $R_c \approx \langle \kappa \rangle^{-1} = B^2/|\mathbf{B} \cdot \nabla \mathbf{B}| \approx (L_r/2)(B^2/B_x^2) \approx L_r$. In summary, the total magnetic energy conversion, field line contraction (Fermi drive), and reconnection rate provide strong evidence for the remarkable similarity of bulk properties of the 2D and 3D reconnection.

V. ELECTRON ACCELERATION

In a previous study¹⁹ we found that electron acceleration was enhanced in a 3D reconnecting system. These results are summarized in Fig. 5. Although there is substantial acceleration in both systems, the fraction of electrons with energy exceeding $0.5m_e c^2$ is more than an order of magnitude larger than in the 2D simulation (Fig. 5a). However, as noted in Section IV, the magnetic energy dissipation is comparable in 2D and 3D systems. This suggests that the increased energetic electron production in the 3D system is due to enhanced acceleration efficiency rather than an increase in the total energy imparted to the plasma. According to equation (1) the acceleration mechanisms have different scalings with the particle energy: the Fermi reflection term is second-order in the parallel velocity, whereas the parallel electric field term is only first-order. The instantaneous average acceler-

ation per particle for both E_{\parallel} and Fermi reflection in configuration SM, ($b_g = 1$) is shown in Fig. 5b. The bulk thermal electrons (low energies) are primarily accelerated by E_{\parallel} , whereas Fermi reflection is more important at high energies. The energetic electrons are primarily accelerated in the parallel direction so that the momentum distribution $f(p_{\parallel})$ exceeds $f(p_{\perp})$ (Fig. 5c), consistent with acceleration via Fermi reflection and E_{\parallel} . To summarize: electron acceleration, primarily driven by field-line contraction, is enhanced in 3D systems. However, this is not due to greater energy release, so must instead be due to enhancement of the acceleration efficiency.

As was discussed in Section IV, the stochastic structure of the magnetic field in 3D systems allows field-line-following particles to wander throughout the chaotic reconnecting region⁴⁶. However, in 2D systems reconnected field lines form closed loops (islands) that trap particles. The impact of topology on transport is reflected in the spatial distribution of the most energetic particles (shown in Fig. 6a,b). These particles occupy narrow bands well inside the islands in the 2D simulation, but are distributed throughout the reconnecting region in the 3D simulation. The most efficient electron acceleration regions are near the X-lines and at the ends of islands (Fig. 6c,d). In the 2D system, trapped energetic particles are unable to access these regions, and the overall acceleration efficiency is suppressed with respect to the 3D system where the energetic particles wander the reconnecting region and undergo continuous acceleration. Figure 6e,f shows the resulting rate of Fermi energization for electrons with $\epsilon > 0.5m_e c^2$, revealing an order-of-magnitude difference between the two systems.

In order to examine the transition from 2D to 3D reconnection, we performed a set of simulations with different values of L_z , from a quasi-2D system with $L_z = 1.6d_i$ to a simulation with $L_z = L_y = 25.6d_i$. Figure 7a-c shows the spatial distribution of the energetic electrons ($\epsilon > 0.5m_e c^2$) for several of these simulations. Surprisingly, there is a sharp transition at $L_z = 6.4d_i$: below this threshold, energetic electrons are trapped inside islands, whereas above this threshold the energetic electrons are space-filling. Electron energy spectra exhibit the same transition (Fig. 7d). Simulations with $L_z < 6.4d_i$ do not show enhancement with respect to the 2D result, whereas simulations $L_z \geq 6.4d_i$ are consistent with the 3D result. This reinforces the correlation between enhanced transport and acceleration in 3D systems.

VI. THE ROLE OF THE GUIDE FIELD

In a recent study of two-dimensional kinetic reconnection (Dahlin et al., 2016²³), we found that the magnetic guide field was a vital parameter that controls the efficiency of electron acceleration. In a system with a guide field much smaller than the reconnecting component, the dominant electron accelerator was a Fermi-type mechanism that preferentially energizes the most energetic particles. In the strong guide field regime, however, the field-line contraction that drives Fermi reflection was negligible. Instead, parallel electric fields (E_{\parallel}) were primarily responsible for driving electron heating. Electron acceleration was suppressed in the systems with a strong guide field. We argued that this was due to the weaker energy scaling of E_{\parallel} acceleration.

To probe the role of the guide field in three-dimensional transport and particle acceleration, we performed several three-dimensional simulations in the configuration SM with $0 \leq b_g \leq 1.5$ and compared these results with a set of quasi-2D simulations ($L_z = 1.6d_i$). Selected electron energy spectra from these simulations are shown in Figure 8a-c. Figure 8d shows the number of electrons exceeding $30T_0$, revealing that energetic electron production varies strongly with the guide field. The efficiency of the Fermi mechanism that drives energetic electron production weakens with increasing guide field²³. The quasi-2D spectra (Fig. 8c) are consistent with this result, explaining why the energetic electron production diminishes as $b_g > 1$. The decreasing energetic electron production for $b_g \ll 1$ must then be due to three-dimensional effects. Indeed, Fig. 8b shows that the relative 3D enhancement (f_{3D}/f_{2D}) increases with b_g until it saturates above $b_g = 1$ (there is little difference between $b_g = 1, 1.5$).

Representative field lines for several of the 3D simulations are shown in Fig. 10, illustrating the differing field line structures (Fig. 10a shows field lines from a 2D simulation). In Fig. 10b, the field lines are clearly stochastic, and do not show clear flux rope structures that would trap particles; hence, electrons are free to return to acceleration regions. In weak guide-field reconnection, however (Figs. 10c-d), field lines wrap around clearly-defined flux ropes, and in the case with $b_g = 0$, the field lines approximately close on themselves. This structure inhibits particle escape from islands, similar to the 2D structure shown in Fig. 10a, where flux surfaces are closed and particles become topologically disconnected from acceleration regions. In 3D, the guide field plays a role in breaking the 2D symmetry and

allowing particles to escape along the flux rope axis. This explains why the three-dimensional enhancement increases with the guide field. The saturation above $b_g = 1$ can be explained by noting that magnetic structures are typically elongated along the guide field for $b_g > 1$ so that particles must move farther along the axis to escape the island. Hence, further 3D enhancement over what is shown in Fig. 8b should not occur.

The convolution of the Fermi acceleration efficiency and the effectiveness of three-dimensional transport results in a peak energetic electron production at $b_g \approx 0.6$. Results from a set of 3D simulations with $L_x \times L_y \times L_z = 102.4 \times 51.2 \times 25.6$ (configuration SL) are shown in Fig. 9 (dashed lines indicate an earlier time). These simulations show that the enhancement f_{3D}/f_{2D} increases as the spectra extend to higher energies, suggesting that three-dimensional transport will be even more important in physical systems such as the corona where the length scales $L \gg d_i$. The most efficient guide field, in these simulations $b_g \approx 0.6$, will likely depend both on the system size and on other plasma parameters such as the plasma beta, which can impact the relative efficiency of Fermi and E_{\parallel} -driven acceleration.

VII. AN ‘INJECTION CRITERION’ FOR ENHANCED ACCELERATION

A limitation of the present simulations is the use of an artificial mass ratio, which reduces the separation between proton and electron scales. To examine how the mass ratio impacts particle acceleration, we performed simulations with $m_i/m_e = 1, 25, 100$ (configurations S1, SM, and S100) and $b_g = 1$. Figure 11 shows the relative enhancement of the energy spectra in the three-dimensional simulations (f_{3D}/f_{2D}). For the electron-positron case ($m_i/m_e = 1$), there is only a slight enhancement (~ 2) in the energetic tail for both species. For the electron-proton cases ($m_i/m_e = 25, 100$), the energetic electrons are enhanced whereas the energetic ions are suppressed. The enhancement (suppression) of the energetic electrons (ions) is greater for the more realistic mass ratio. This trend, along with the weak enhancement for the electron-positron case, suggesting that the separation of scales between species plays an important role in 3D particle acceleration and that the impact of 3D transport should be robust for the physical mass ratio.

We propose the following explanation: in order for a charged particle to accelerate multiple times, it must propagate upstream against the Alfvénic outflow that ejects plasma

from the energy release regions near the X-line and at the ends of islands. The condition $v/c_A \gg 1$ then acts as an ‘injection criterion’ for efficient acceleration (this is analogous to the injection problem in shock-driven particle acceleration). Heavy species (protons for $m_i/m_e > 1$, and both electrons and positrons for $m_i/m_e = 1$) are responsible for the bulk inertia and hence the reconnection outflow velocity c_A . The characteristic velocity of these particles is therefore of the same order as the Alfvén speed ($v \sim c_A$), so that the bulk particles do not meet the injection criterion and do not experience enhanced 3D acceleration. A few particles in the tail of the distribution satisfy the criterion in the electron-positron case, explaining the small (~ 2) enhancement at high energies. For the electron-proton simulations ($m_i/m_e = 25, 100$) the electron thermal velocity $v_{th,e}/c_A \sim \sqrt{\beta_x(m_i/m_e)} \gg 1$ greatly exceeds the Alfvén speed. Recent numerical studies suggest that even in environments with $\beta \ll 1$, reconnection heats electrons to an appreciable fraction of the available magnetic energy density^{47,48}: $\Delta T_e \approx 0.03 m_e c_{Ae}^2$, corresponding to $v_{th,e}/c_A \approx \sqrt{0.06 m_i/m_e} \approx 10$ so that essentially all reconnection-heated electrons will satisfy the criterion, independent of the initial temperature. In contrast, ions are typically sub-Alfvénic and would require an injection mechanism (e.g.^{49–51}) to undergo continuous acceleration. However, the suppression of ion acceleration in 3D systems is surprising. While the relative increase in energy going into energetic electrons may play some role, it is not clear that this should preferentially impact the energetic ions. Further treatment is beyond the scope of this paper.

The injection criterion may require modification in the large guide field limit ($B_z/B_0 \gg 1$). In this limit, the electrons dominantly stream in the z -direction, so the relevant velocity to compare to the outflow speed is $v_x \approx v B_x/B \approx v/b_g$ so the injection criterion becomes $v/c_A \gg b_g$. In strongly relativistic systems, all velocities approach c , so that the injection criterion cannot be met. This suggests that enhanced 3D acceleration should not occur for relativistic reconnection in either pair^{26,36} or electron-proton plasmas.

VIII. DISCUSSION

Electron acceleration in three-dimensional systems is a complex problem that intrinsically depends on the transport properties of reconnection-generated magnetic fields. The picture that emerges from this set of simulations is that particle acceleration is efficient in a three-dimensional system when the energetic population can freely access acceleration sites and

thereby achieve continuous energy gain. This requires both topological access to energy release regions and a super-Alfvénic particle velocity in order to explore the open topology at a faster time scale than the system evolves (most easily understood as the ejection of flux from the X-line). While electrons satisfy this condition rather easily, heavy species such as protons would require an injection mechanism in order to be able to propagate upstream against the reconnection outflow.

Efficient transport requires a strong guide field. The field structure in antiparallel reconnection is quasi-laminar, so that energetic particles are still well-trapped in islands. Propagation upstream against the Alfvén velocity is not possible in strongly relativistic reconnection, where all characteristic velocities approach the speed of light. This is consistent with studies by Guo et al.^{26,52,53}, that exhibit no substantial difference in energetic particle production between two and three-dimensional simulations in the relativistic regime.

The nonthermal electron spectra in both simulations do not assume a power law form as is frequently observed in nature. The maximum energy gain is limited due to the modest size of the simulations; previous 2D simulations have shown that the total energy gain is greater in larger systems²⁴. An additional issue is that these simulations have periodic boundary conditions that prevent particle loss from the system. Solar observations suggest that electrons are confined in regions of energy release in the corona³; possible mechanisms for this confinement include mirroring and double layers⁵⁴. This could suggest that particle loss is not an important concern. On the other hand, it has been suggested that the development of a power law requires a loss mechanism in addition to an energy drive²². However, several recent simulations suggest that power-law spectra may still develop in the absence of a loss mechanism^{26,27,36,55}. The set of conditions under which power-law spectra form in kinetic reconnection simulations remains an open issue.

The simulations have a number of numerical limitations. These include comparatively small spatial and temporal scales, and an artificial electron-to-proton mass ratio. However, as was discussed in Section VII, the greater characteristic velocity of a realistically ‘light’ electron facilitates transport in the stochastic topology; the efficiency of Fermi acceleration does not directly depend on the particle mass. The largest simulations show that three-dimensional dynamics are increasingly important at larger scales; in contrast the diminishing frequency of island mergers leads to suppression of further acceleration in two-dimensional systems.

The role of the guide field in magnetic reconnection has broad implications for reconnection-driven particle acceleration in astrophysical systems. Electron acceleration is most efficient in the regime where both (a) the Fermi mechanism operates and (b) strong three-dimensional transport exists. The former requires $b_g \lesssim 1$, the latter $b_g > 0$, suggesting that reconnection with a magnetic field of the same order as the reconnecting component ($b_g \sim 1$) will yield the most efficient energetic electron production. This result is especially relevant for solar flares, where the shear in the magnetic configuration typically diminishes during the impulsive phase (see Fletcher et al.⁵⁶ and references therein). This corresponds to a transition from strong to weak guide field reconnection, and could explain why electron acceleration (as inferred from hard X-ray emissions) is typically confined to the impulsive phase.

ACKNOWLEDGMENTS

This work has been supported by NSF Grants AGS1202330 and PHY1102479, and NASA grants NNX11AQ93H, APL-975268, NNX08AV87G, NAS 5- 98033, and NNX08AO83G. J.T.D. acknowledges support from the NASA LWS Jack Eddy Fellowship administered by the University Corporation for Atmospheric Research in Boulder, Colorado. Simulations were carried out at the National Energy Research Scientific Computing Center.

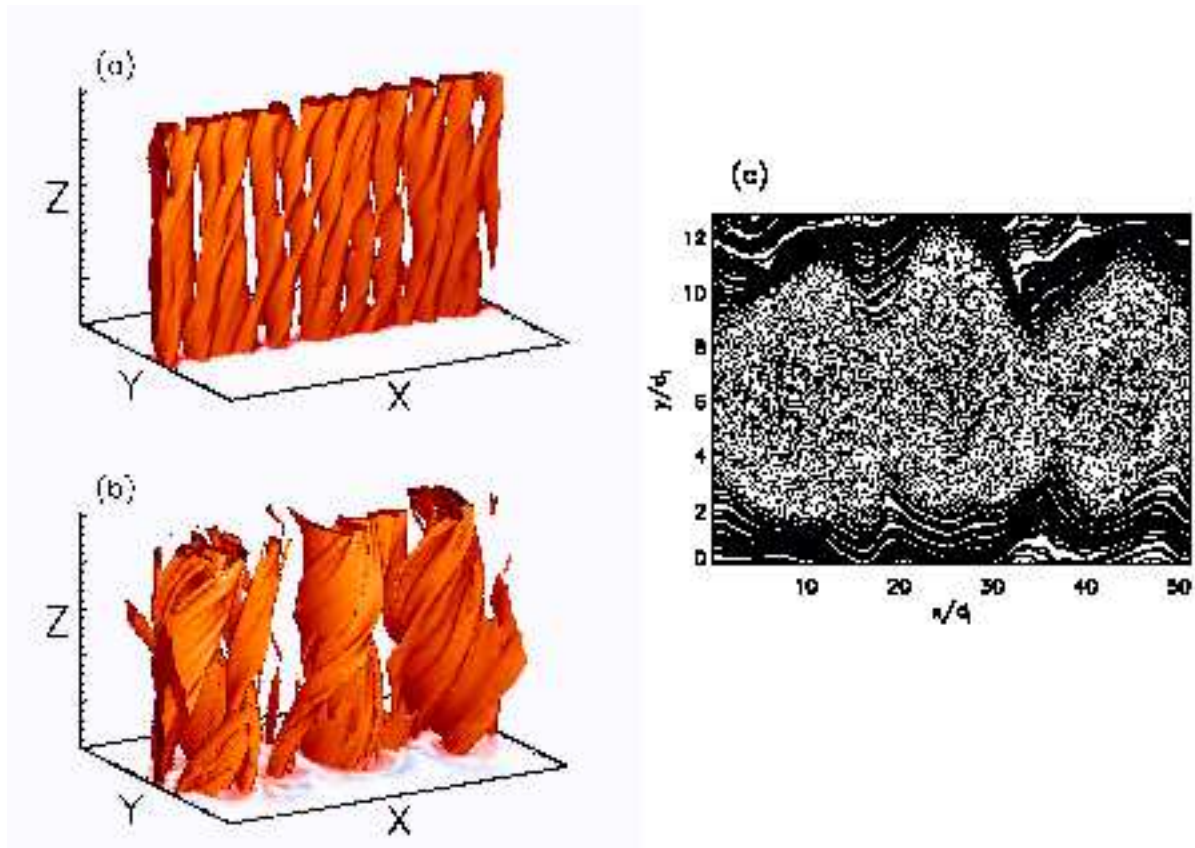


FIG. 1. Results for configuration SM. (a,b) Isosurfaces of J_{ez} at $\Omega_{cit} = 12, 50$ respectively, illustrating the nonlinear filamentary current structure. (c) Poincaré surface-of-section at $\Omega_{cit} = 50$. We trace a set of field lines beginning at $x = 0$, $0 < y < 12.8$, $z = 0$ and plot where they puncture the plane $z = 0$. The surface-of-section shows a clear boundary between the stochastic field lines inside the reconnecting region and the laminar unreconnected fields.

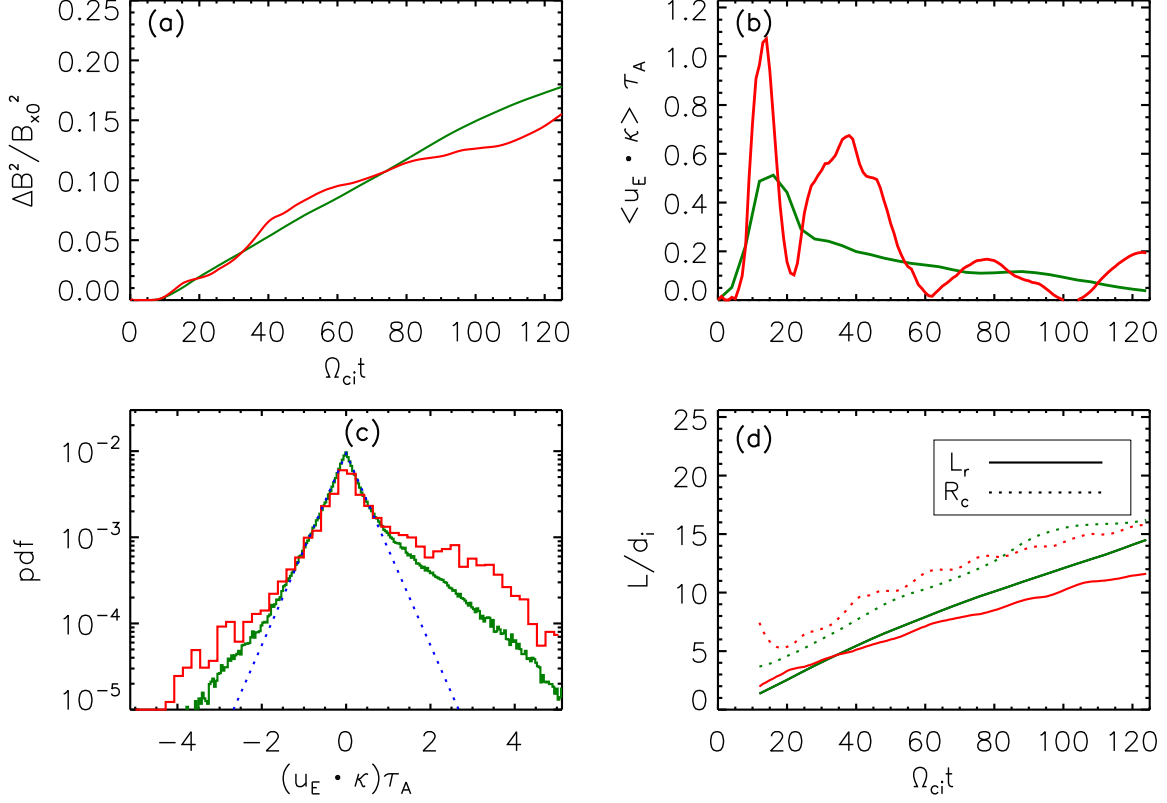


FIG. 2. Results for configuration SL: 3D (green) and 2D (red). (a) Magnetic energy release vs. time. (b) Spatially averaged $(\mathbf{u}_E \cdot \boldsymbol{\kappa})\tau_A$ over the reconnecting region, where $\tau_A = L_x/c_A$ is the Alfvén crossing time. (c) Probability distribution function of $(\mathbf{u}_E \cdot \boldsymbol{\kappa})\tau_A$ at $\Omega_{ci}t = 40$, with a superimposed double-exponential fit (blue dotted line). (d) Reconnection region half-width L_r and radius of curvature R_c .

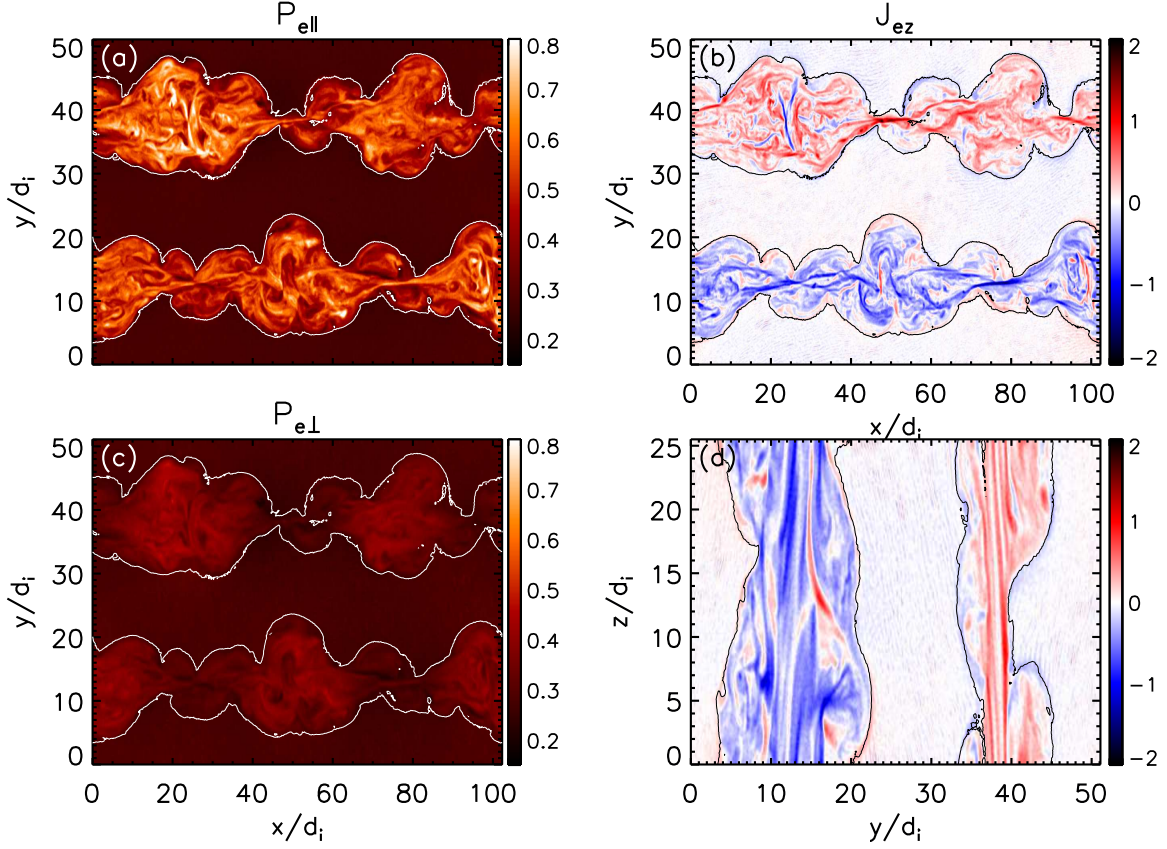


FIG. 3. Results for configuration SL. (a)(c) $z = 0$ slices at $\Omega_{ci}t = 100$ of parallel and perpendicular electron pressure. (b) (d) z -directed electron current density in planes defined by $z = 0$ and $x = 0$, respectively. White and black outlines indicate the contour $P_{e\parallel,nt} = 0.04n_0T_{e0}$, a marker for the region of reconnected magnetic field.

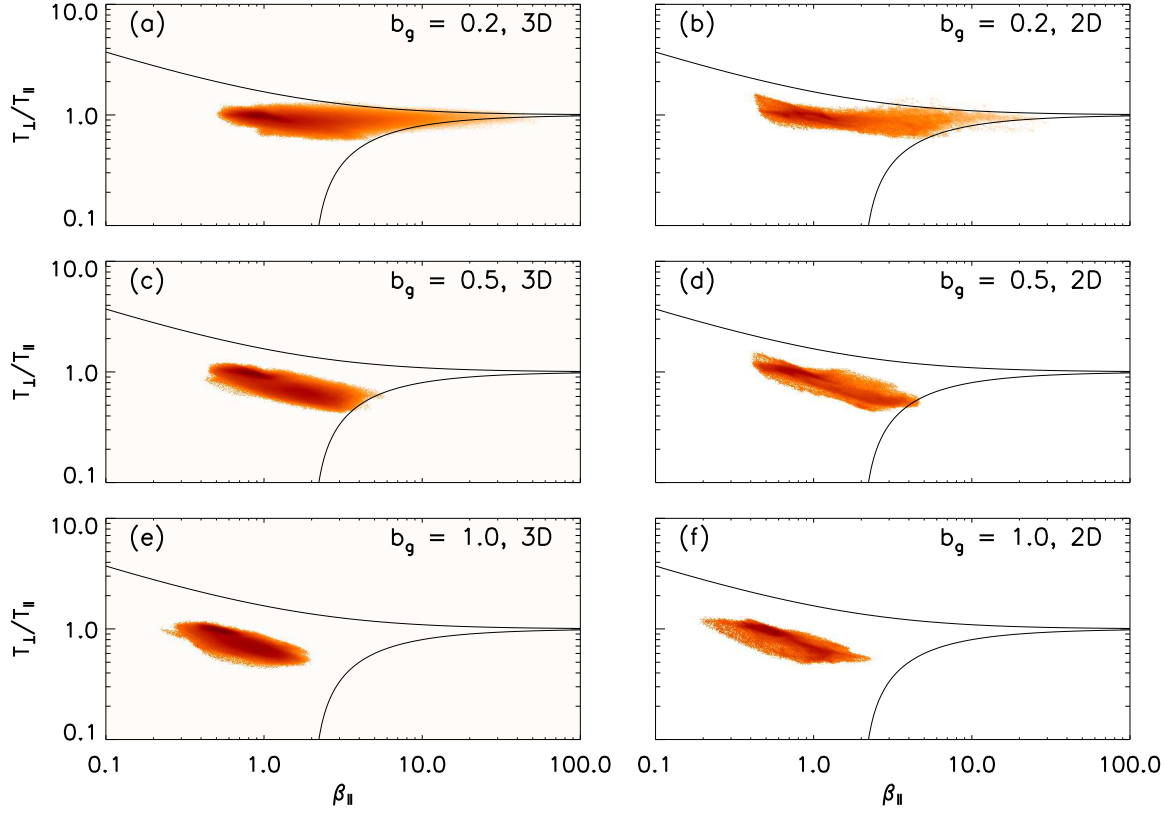


FIG. 4. Results for configuration SM. Phase space distribution of temperature ratio T_{\perp}/T_{\parallel} vs. β_{\parallel} . Black lines indicate marginal stability conditions for the ideal firehose (bottom) and mirror (top) instabilities.

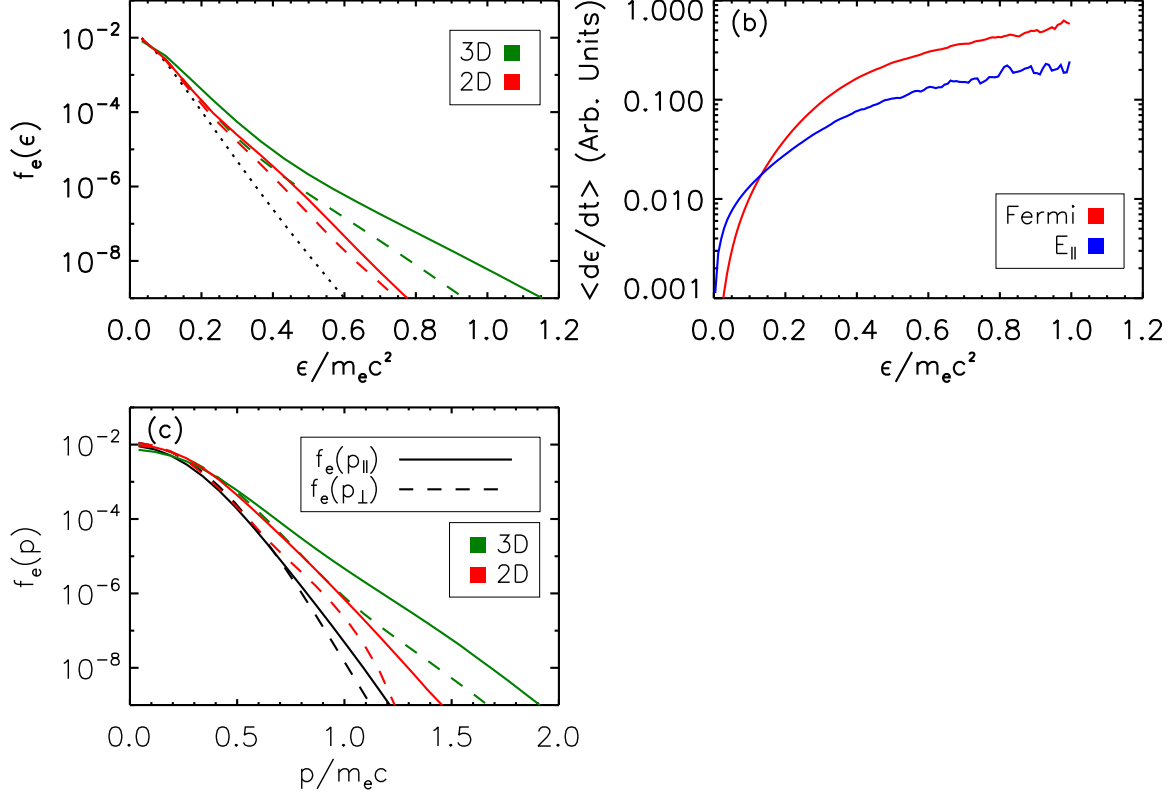


FIG. 5. Results for configuration SL: 3D (green) and 2D (red). (a) Energetic spectra at $\Omega_{ci}t = 50$ (dashed) and 125 (solid) (b) Average energy gain due to Fermi acceleration (red) and E_{\parallel} (blue) in simulation 4a at $\Omega_{ci}t = 100$. (c) Parallel and perpendicular momentum spectra at $\Omega_{ci}t = 0, 125$.

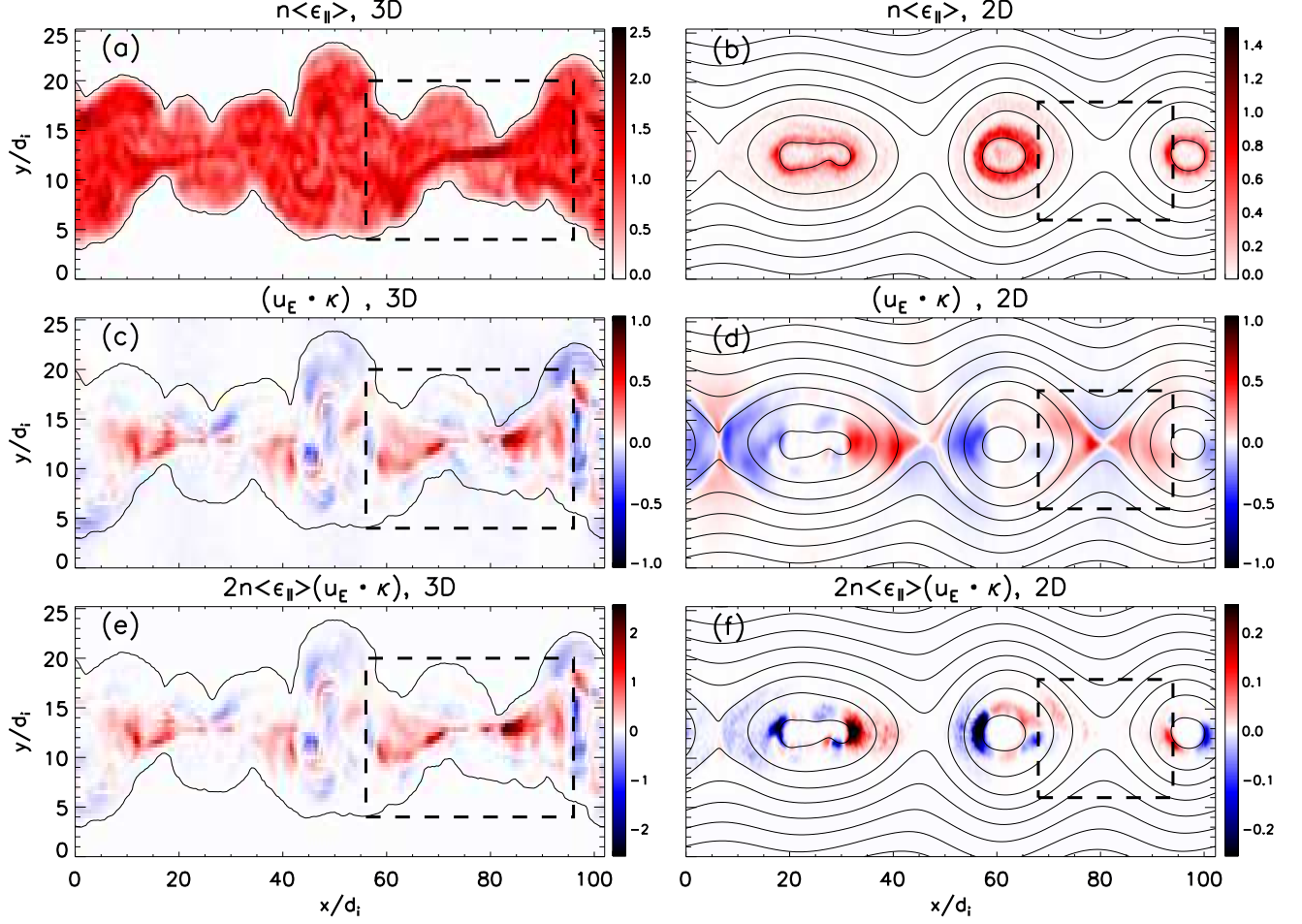


FIG. 6. Results for configuration SL: 3D (left) and 2D (right) at $\Omega_{ci}t = 100$ in the plane $z = 0$. (a-b) Parallel energy density for electrons with $\epsilon > 0.5m_e c^2$. (c-d) Field-line contraction rate $\mathbf{u}_E \cdot \boldsymbol{\kappa}$. (e-f) Fermi acceleration for electrons with $\epsilon > 0.5m_e c^2$. The similarity between (c) and (e) reflects the nearly uniform spatial distribution of the energetic electrons in the reconnecting region. Dashed boxes outline one X-line in each panel.

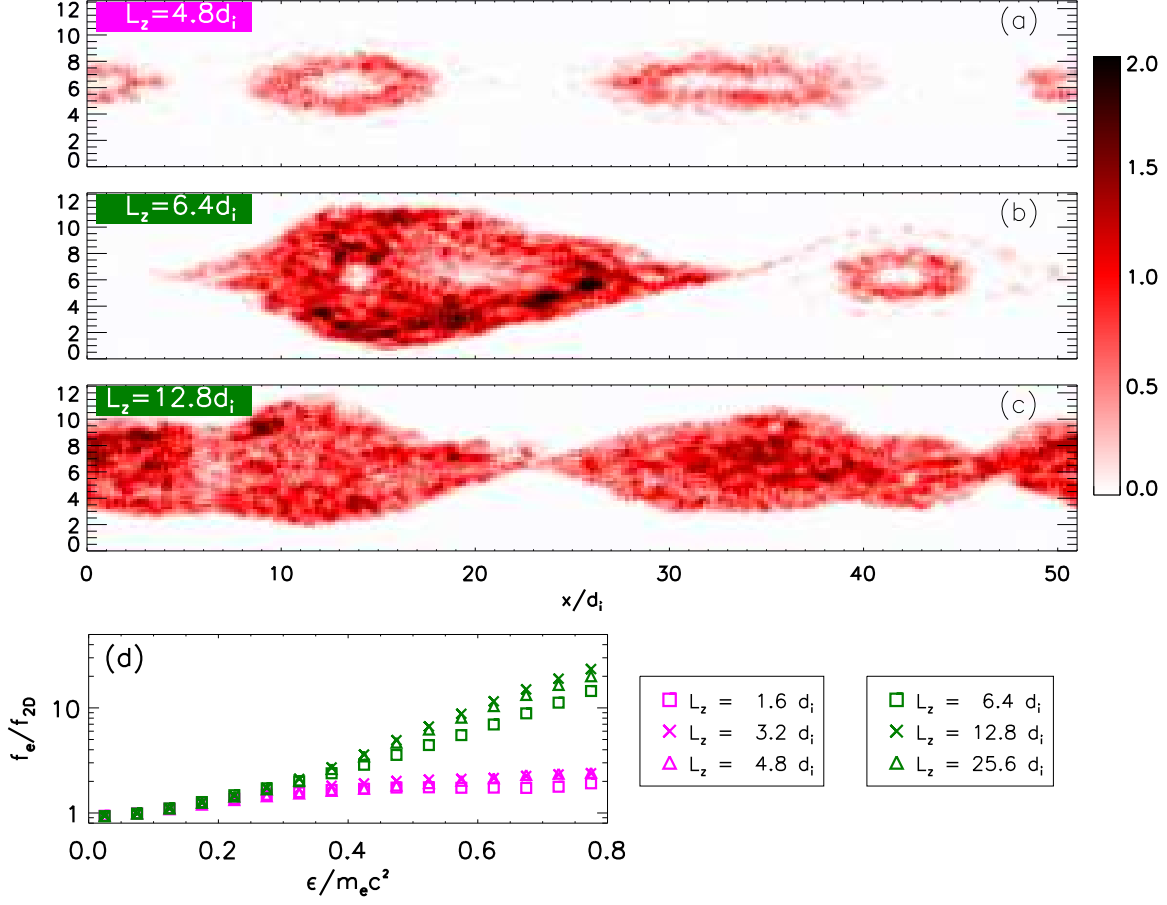


FIG. 7. Results for configuration SM, $b_g = 1$. (a-c) Spatial distribution of electrons with $\epsilon > 0.5 m_e c^2$. (d) Electron energy spectra normalized to the 2D spectrum at $\Omega_{ci} t = 50$.

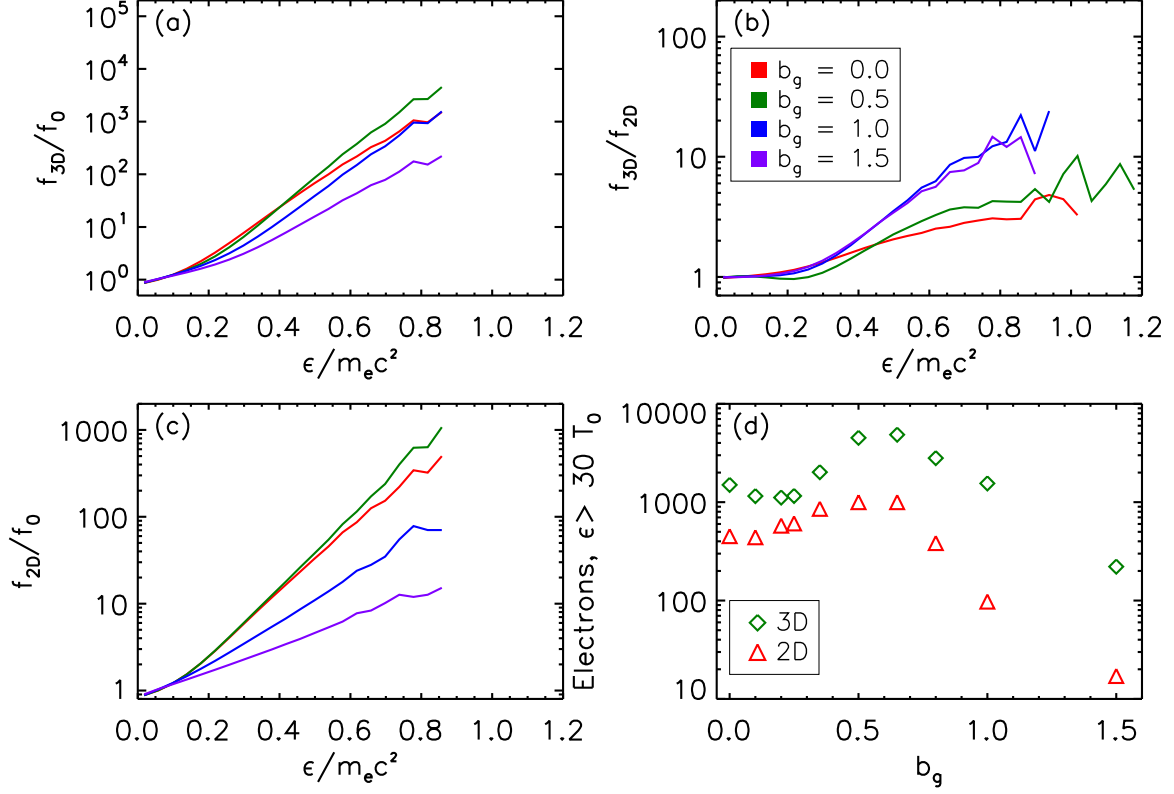


FIG. 8. Results for configuration SM at $\Omega_{ci}t = 50$. Three-dimensional electron energy spectra f_{3D} normalized to the initial spectrum f_0 (a) and quasi-2D spectra f_{2D} (b). (c) quasi-2D spectra f_{2D} normalized to the initial spectrum f_0 . (d) Electrons exceeding $30T_{e0}$ vs. guide field. The system with $b_g = 0.65$ generates the greatest number of energetic electrons.

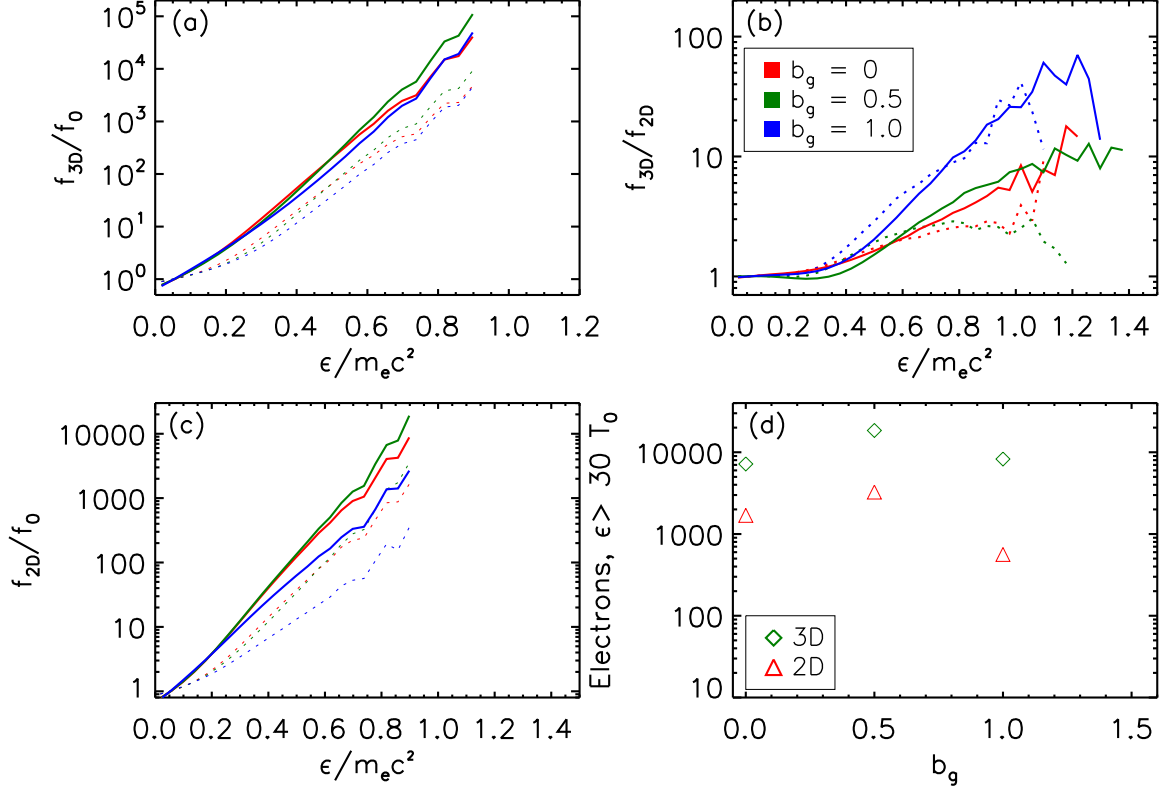


FIG. 9. Results for configuration SL. Three-dimensional electron energy spectra normalized to the initial spectrum (a) and quasi-2D spectra (b) at $\Omega_{ci}t = 125$ (solid) and $\Omega_{ci}t = 50$ (dashed). (c) quasi-2D spectra normalized to the initial ($t = 0$) spectrum. (d) Electrons exceeding $30T_{e0}$ at $\Omega_{ci}t = 50$ vs. guide field. The system with $b_g = 0.5$ generates the greatest number of energetic electrons.

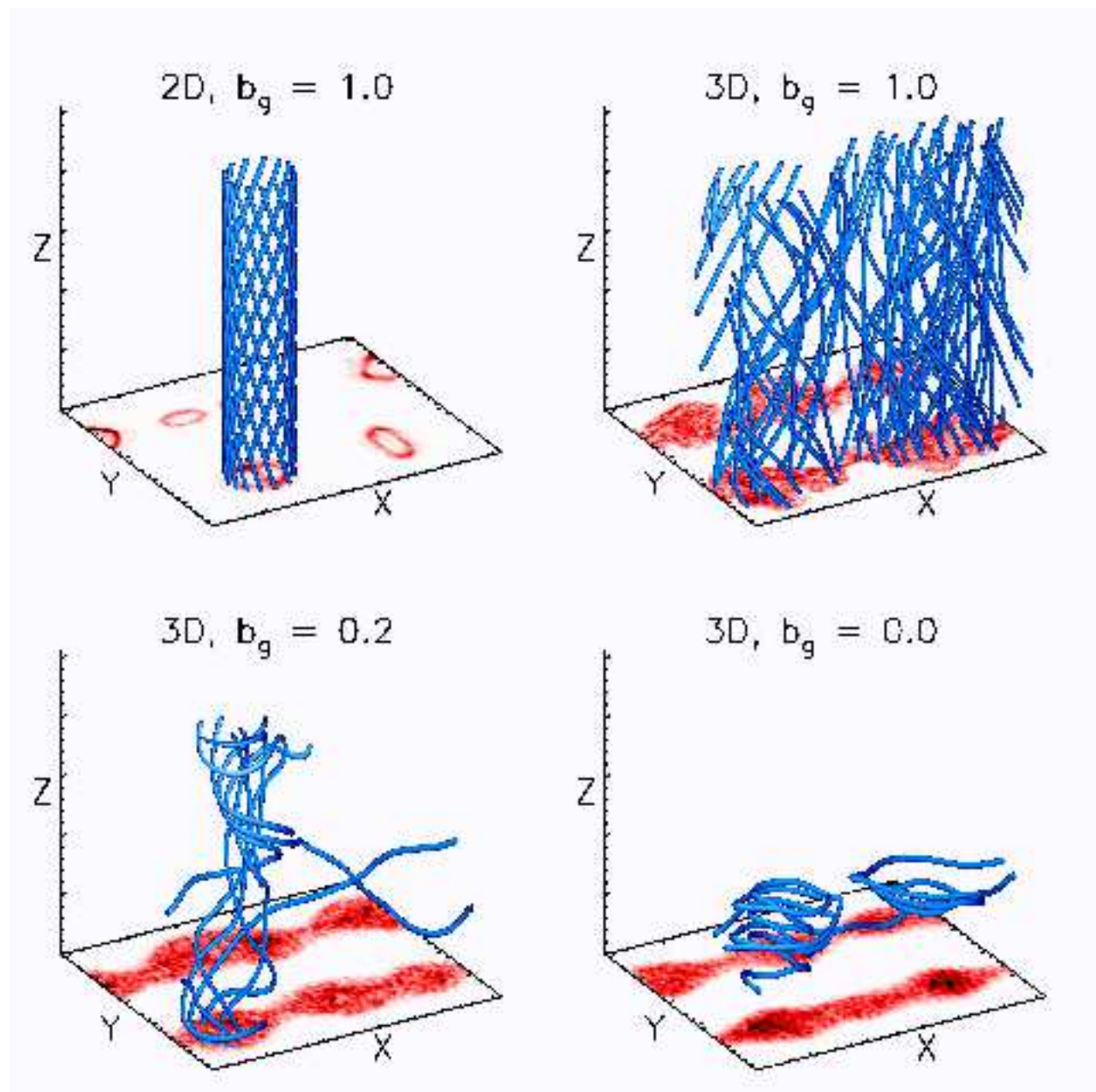


FIG. 10. Results from configuration SM. Single field lines (blue) for simulations with different guide fields. Two-dimensional ($z = 0$) slices of the energetic electron density are shown at the bottom of each panel.

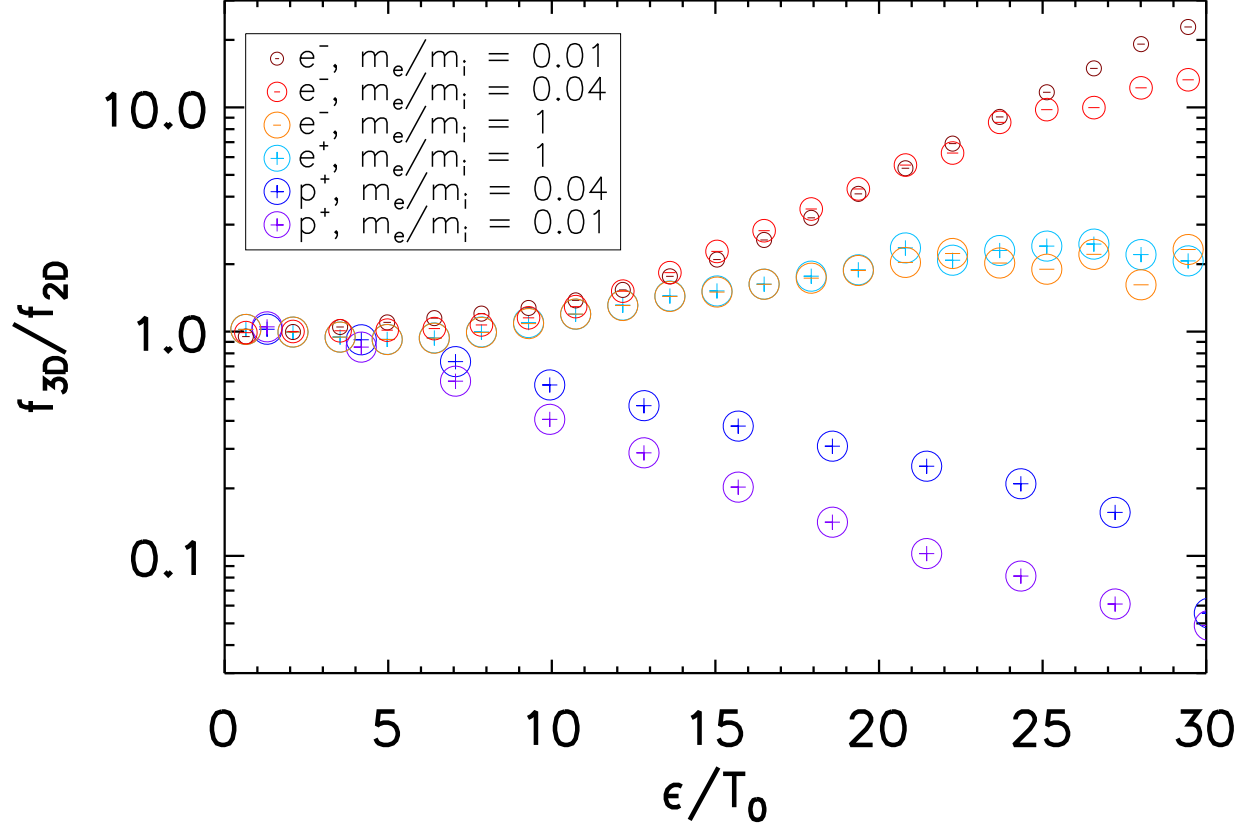


FIG. 11. Results from configurations SM, S1, and S100. Three-dimensional enhancement (f_{3D}/f_{2D}) for simulations with different mass ratios m_i/m_e . For the pair plasma ($m_i/m_e = 1$), both species exhibit a small enhancement ~ 2 , whereas for simulations with $m_i \gg m_e$, energetic electrons are enhanced whereas energetic ions are suppressed.

REFERENCES

- ¹R. P. Lin, S. Krucker, G. J. Hurford, D. M. Smith, H. S. Hudson, G. D. Holman, R. A. Schwartz, B. R. Dennis, G. H. Share, R. J. Murphy, A. G. Emslie, C. Johns-Krull, and N. Vilmer, *Ap. J.* **595**, L69 (2003).
- ²M. Øieroset, R. P. Lin, T. D. Phan, D. E. Larson, and S. D. Bale, *Phys. Rev. Lett.* **89**, 195001 (2002).
- ³S. Krucker, H. S. Hudson, L. Glesener, S. M. White, S. Masuda, J.-P. Wuelser, and R. P. Lin, *Ap. J.* **714**, 1108 (2010).
- ⁴M. Oka, S. Ishikawa, P. Saint-Hilaire, S. Krucker, and R. P. Lin, *The Astrophysical Journal* **764**, 6 (2013).
- ⁵G. Drenkhahn and H. C. Spruit, *Astronomy & Astrophysics* **391**, 1141 (2002).
- ⁶F. C. Michel, *Ap. J.* **431**, 397 (1994).
- ⁷M. Tavani, A. Bulgarelli, V. Vittorini, A. Pellizzoni, E. Striani, P. Caraveo, M. C. Weiskopf, A. Tennant, G. Pucella, A. Trois, E. Costa, Y. Evangelista, C. Pittori, F. Verrecchia, E. Del Monte, R. Campana, M. Pilia, A. De Luca, I. Donnarumma, D. Horns, C. Ferrigno, C. O. Heinke, M. Trifoglio, F. Gianotti, S. Vercellone, A. Argan, G. Barbiellini, P. W. Cattaneo, A. W. Chen, T. Contessi, F. DAmmando, G. DeParis, G. Di Cocco, G. Di Persio, M. Feroci, A. Ferrari, M. Galli, A. Giuliani, M. Giusti, C. Labanti, I. Lashov, F. Lazzarotto, P. Lipari, F. Longo, F. Fuschino, M. Marisaldi, S. Mereghetti, E. Morelli, E. Moretti, A. Morselli, L. Pacciani, F. Perotti, G. Piano, P. Picozza, M. Prest, M. Rapisarda, A. Rappoldi, A. Rubini, S. Sabatini, P. Soffitta, E. Vallazza, A. Zambra, D. Zanello, F. Lucarelli, P. Santolamazza, P. Giommi, L. Salotti, and G. F. Bignami, *Science* **331**, 736 (2011).
- ⁸A. A. Abdo, M. Ackermann, M. Ajello, A. Allafort, L. Baldini, J. Ballet, G. Barbiellini, D. Bastieri, K. Bechtol, R. Bellazzini, B. Berenji, R. D. Blandford, E. D. Bloom, E. Bonamente, A. W. Borgland, A. Bouvier, T. J. Brandt, J. Bregeon, A. Brez, M. Brigida, P. Bruel, R. Buehler, S. Buson, G. A. Caliandro, R. A. Cameron, A. Cannon, P. A. Caraveo, J. M. Casandjian, . elik, E. Charles, A. Chekhtman, C. C. Cheung, J. Chiang, S. Ciprini, R. Claus, J. Cohen-Tanugi, L. Costamante, S. Cutini, F. DAmmando, C. D. Dermer, A. de Angelis, A. de Luca, F. de Palma, S. W. Digel, E. do Couto e Silva, P. S. Drell, A. Drlica-Wagner, R. Dubois, D. Dumora, C. Favuzzi, S. J. Fegan, E. C. Ferrara, W. B.

- Focke, P. Fortin, M. Frailis, Y. Fukazawa, S. Funk, P. Fusco, F. Gargano, D. Gasparrini, N. Gehrels, S. Germani, N. Giglietto, F. Giordano, M. Giroletti, T. Glanzman, G. Godfrey, I. A. Grenier, M.-H. Grondin, J. E. Grove, S. Guiriec, D. Hadasch, Y. Hanabata, A. K. Harding, K. Hayashi, M. Hayashida, E. Hays, D. Horan, R. Itoh, G. Jhannesson, A. S. Johnson, T. J. Johnson, D. Khangulyan, T. Kamae, H. Katagiri, J. Kataoka, M. Kerr, J. Knudsen, M. Kuss, J. Lande, L. Latronico, S.-H. Lee, M. Lemoine-Goumard, F. Longo, F. Loparco, P. Lubrano, G. M. Madejski, A. Makeev, M. Marelli, M. N. Mazziotta, J. E. McEnery, P. F. Michelson, W. Mitthumsiri, T. Mizuno, A. A. Moiseev, C. Monte, M. E. Monzani, A. Morselli, I. V. Moskalenko, S. Murgia, T. Nakamori, M. Naumann-Godo, P. L. Nolan, J. P. Norris, E. Nuss, T. Ohsugi, A. Okumura, N. Omodei, J. F. Ormes, M. Ozaki, D. Paneque, D. Parent, V. Pelassa, M. Pepe, M. Pesce-Rollins, M. Pierbattista, F. Piron, T. A. Porter, S. Rain, R. Rando, P. S. Ray, M. Razzano, A. Reimer, O. Reimer, T. Reposeur, S. Ritz, R. W. Romani, H. F.-W. Sadrozinski, D. Sanchez, P. M. S. Parkinson, J. D. Scargle, T. L. Schalk, C. Sgr, E. J. Siskind, P. D. Smith, G. Spandre, P. Spinelli, M. S. Strickman, D. J. Suson, H. Takahashi, T. Takahashi, T. Tanaka, J. B. Thayer, D. J. Thompson, L. Tibaldo, D. F. Torres, G. Tosti, A. Tramacere, E. Troja, Y. Uchiyama, J. Vandenbroucke, V. Vasileiou, G. Vianello, V. Vitale, P. Wang, K. S. Wood, Z. Yang, and M. Ziegler, *Science* **331**, 739 (2011).
- ⁹M. Hoshino, T. Mukai, T. Terasawa, and I. Shinohara, *J. Geophys. Res.* **106**, 25,979 (2001).
- ¹⁰S. Zenitani and M. Hoshino, *Ap. J. Lett.* **562**, L63 (2001).
- ¹¹J. F. Drake, M. A. Shay, W. Thongthai, and M. Swisdak, *Phys. Rev. Lett.* **94**, 095001 (2005).
- ¹²P. L. Pritchett, *J. Geophys. Res.* **111**, A10212 (2006), 10.1029/2006JA011793.
- ¹³J. Egedal, W. Daughton, J. F. Drake, N. Katz, and A. Lê, *Phys. Plasmas* **16**, 050701 (2009), 10.1063/1.3130732.
- ¹⁴M. Oka, T.-D. Phan, S. Krucker, M. Fujimoto, and I. Shinohara, *Ap. J.* **714**, 915 (2010).
- ¹⁵M. Hoshino, *Phys. Rev. Lett.* **108**, 135003 (2012).
- ¹⁶Y. E. Litvinenko, *Ap. J.* **462**, 997 (1996).
- ¹⁷D. A. Uzdensky, B. Cerutti, and M. C. Begelman, *The Astrophysical Journal Letters* **737**, L40 (2011).
- ¹⁸J. Egedal, W. Daughton, and A. Lê, *Nature Phys.* **8**, 321 (2012).

- ¹⁹J. T. Dahlin, J. F. Drake, and M. Swisdak, *Physics of Plasmas* **22**, 100704 (2015), <http://dx.doi.org/10.1063/1.4933212>.
- ²⁰J. F. Drake, M. Swisdak, H. Che, and M. A. Shay, *Nature* **443**, 553 (2006).
- ²¹J. F. Drake, M. Opher, M. Swisdak, and J. N. Chamoun, *Ap. J.* **709**, 963 (2010).
- ²²J. F. Drake, M. Swisdak, and R. Fermo, *The Astrophysical Journal Letters* **763**, L5 (2013).
- ²³J. T. Dahlin, J. F. Drake, and M. Swisdak, *Phys. Plasmas* (2016), submitted, arXiv:1607.03857.
- ²⁴J. T. Dahlin, J. F. Drake, and M. Swisdak, *Phys. Plasmas* **21**, 092304 (2014).
- ²⁵H. Wang, Q. Lu, C. Huang, and S. Wang, *The Astrophysical Journal* **821**, 84 (2016).
- ²⁶F. Guo, H. Li, W. Daughton, and Y.-H. Liu, *Phys. Rev. Lett.* **113**, 155005 (2014).
- ²⁷X. Li, F. Guo, H. Li, and G. Li, *The Astrophysical Journal Letters* **811**, L24 (2015).
- ²⁸R. Numata and N. F. Loureiro, *Journal of Plasma Physics* **81**, 305810201 (17 pages) (2015).
- ²⁹L.-J. Chen, A. Bhattacharjee, P. A. Puhl-Quinn, H. Yang, N. Bessho, S. Imada, S. Mühlbachler, P. W. Daly, B. Lefebvre, Y. Khotyaintsev, A. Vaivads, A. Fazakerley, and E. Georgescu, *Nature Physics* **4**, 19 (2008).
- ³⁰A. Retinò, R. Nakamura, A. Vaivads, Y. Khotyaintsev, T. Hayakawa, K. Tanaka, S. Kasahara, M. Fujimoto, I. Shinohara, J. P. Eastwood, M. Andr, W. Baumjohann, P. W. Daly, E. A. Kronberg, and N. Cornilleau-Wehrin, *Journal of Geophysical Research: Space Physics* **113** (2008), [10.1029/2008JA013511](https://doi.org/10.1029/2008JA013511), a12215.
- ³¹S. Y. Huang, A. Vaivads, Y. V. Khotyaintsev, M. Zhou, H. S. Fu, A. Retin, X. H. Deng, M. Andr, C. M. Cully, J. S. He, F. Sahraoui, Z. G. Yuan, and Y. Pang, *Geophysical Research Letters* **39** (2012), [10.1029/2012GL051946](https://doi.org/10.1029/2012GL051946), l11103.
- ³²R. Schreier, M. Swisdak, J. F. Drake, and P. A. Cassak, *Phys. Plasmas* **17**, 110704 (2010), [10.1063/1.3494218](https://doi.org/10.1063/1.3494218).
- ³³W. Daughton, V. Roytershteyn, H. Karimabadi, L. Yin, B. J. Albright, B. Bergen, and K. J. Bowers, *Nature Phys.* **7**, 539 (2011).
- ³⁴M. Onofri, H. Isliker, and L. Vlahos, *Phys. Rev. Lett.* **96**, 151102 (2006), [10.1103/PhysRevLett96.151102](https://doi.org/10.1103/PhysRevLett96.151102).
- ³⁵G. Kowal, E. M. de Gouveia Dal Pino, and A. Lazarian, *The Astrophysical Journal* **735**, 102 (2011).
- ³⁶L. Sironi and A. Spitkovsky, *The Astrophysical Journal Letters* **783**, L21 (2014).
- ³⁷T. G. Northrop, *Reviews of Geophysics* **1**, 283 (1963).

- ³⁸A. Zeiler, D. Biskamp, J. F. Drake, B. N. Rogers, M. A. Shay, and M. Scholer, *J. Geophys. Res.* **107**, 1230 (2002).
- ³⁹N. A. Bobrova, S. V. Bulanov, J. I. Sakai, and D. Sugiyama, *Physics of Plasmas* **8** (2001).
- ⁴⁰H. P. Furth, J. Killeen, and M. N. Rosenbluth, *Physics of Fluids* **6** (1963).
- ⁴¹A. B. Rechester and M. N. Rosenbluth, *Phys. Rev. Lett.* **40**, 38 (1978).
- ⁴²W. Daughton, T. K. M. Nakamura, H. Karimabadi, V. Roytershteyn, and B. Loring, *Physics of Plasmas* **21**, 052307 (2014), <http://dx.doi.org/10.1063/1.4875730>.
- ⁴³K. M. Schoeffler, J. F. Drake, and M. Swisdak, *Ap. J.* **743**, 70 (2011).
- ⁴⁴J. C. Kasper, A. J. Lazarus, and S. P. Gary, *Geophysical Research Letters* **29**, 20 (2002), 1839.
- ⁴⁵S. D. Bale, J. C. Kasper, G. G. Howes, E. Quataert, C. Salem, and D. Sundkvist, *Phys. Rev. Lett.* **103**, 211101 (2009), [10.1103/PhysRevLett.103.211101](https://doi.org/10.1103/PhysRevLett.103.211101).
- ⁴⁶J. R. Jokipii and E. N. Parker, *The Astrophysical Journal* **155**, 777 (1969).
- ⁴⁷M. A. Shay, C. C. Haggerty, T. D. Phan, J. F. Drake, P. A. Cassak, P. Wu, M. Oieroset, M. Swisdak, and K. Malakit, *Phys. Plasmas* **21**, 122902 (2014).
- ⁴⁸C. C. Haggerty, M. A. Shay, J. F. Drake, T. D. Phan, and C. T. McHugh, *Geophysical Research Letters* **42**, 9657 (2015), [2015GL065961](https://doi.org/10.1029/2015GL065961).
- ⁴⁹J. F. Drake, M. Swisdak, T. D. Phan, P. A. Cassak, M. A. Shay, S. T. Lepri, R. P. Lon, E. Quataert, and T. H. Zurbuchen, *J. Geophys. Res.* **114**, A05111 (2009), [10.1029/2008JA013701](https://doi.org/10.1029/2008JA013701).
- ⁵⁰J. F. Drake, P. A. Cassak, M. A. Shay, M. Swisdak, and E. Quataert, *Ap. J.* **700**, L16 (2009).
- ⁵¹K. Knizhnik, M. Swisdak, and J. Drake, *Ap. J. Lett.* **743** (2011), [10.1088/2041-8205/743/2/L35](https://doi.org/10.1088/2041-8205/743/2/L35).
- ⁵²F. Guo, Y.-H. Liu, W. Daughton, and H. Li, *The Astrophysical Journal* **806**, 167 (2015).
- ⁵³F. Guo, H. Li, W. Daughton, X. Li, and Y.-H. Liu, *Physics of Plasmas* **23**, 055708 (2016), <http://dx.doi.org/10.1063/1.4948284>.
- ⁵⁴T. C. Li, J. F. Drake, and M. Swisdak, *The Astrophysical Journal* **757**, 20 (2012).
- ⁵⁵G. R. Werner, D. A. Uzdensky, B. Cerutti, K. Nalewajko, and M. C. Begelman, *The Astrophysical Journal Letters* **816**, L8 (2016).
- ⁵⁶L. Fletcher, B. R. Dennis, H. S. Hudson, S. Krucker, K. Phillips, A. Veronig, M. Battaglia, L. Bone, A. Caspi, Q. Chen, P. Gallagher, P. T. Grigis, H. Ji, W. Liu, R. O. Milligan, and M. Temmer, *Space Science Reviews* **159**, 19 (2011).